Physical Evidence of Stress-Induced Conformational Changes in Polymers

N. Huynh & G. Youssef

Experimental Mechanics
An International Journal Integrating Experimental Methods with the Mechanical Behavior of Materials and Structures

ISSN 0014-4851

Exp Mech
DOI 10.1007/s11340-020-00673-7

Springer

Experimental Mechanics
https://doi.org/10.1007/s11340-020-00673-7

RESEARCH PAPER

Physical Evidence of Stress-Induced Conformational Changes in Polymers

N. Huynh[1] · **G. Youssef**[1]

Received: 6 May 2020 / Accepted: 7 October 2020

Abstract

Background Polymer mechanics and characterization is an active area of research where a keen effort is directed towards gaining a predictive and correlative relationship between the applied loads and the specific conformational motions of the macromolecule chains.
Objective Therefore, the objective of this research is to introduce the preliminary results based on a novel technique to in situ probe the mechanical properties of polymers using non-invasive, non-destructive, and non-contact terahertz spectroscopy.
Methods A dielectric elastomer actuator (DEA) structure is used as the loading mechanism to avoid obscuring the beam path of transmission terahertz time-domain spectroscopy. In DEAs, the applied voltage results in mechanical stresses under the active electrode area with far-reaching stretching in the passive area. Finite element analysis is used to model and simulate the DEA to quantify the induced stresses at the observation site over a voltage range spanning from 0 V to 3000 V. Additionally, a novel analysis technique is introduced based on the Hilbert-Huang transform to exploit the time-domain signals of the ultrathin elastomeric film and to defy the limits set forth by the current state-of-the-art analysis techniques.
Results The computational result shows a nonlinear relationship between the effective stresses and the applied voltage. Analysis of the terahertz time-domain signals shows a shift in the delay times and a decrease in signal peak amplitudes, whereas these characteristics are implicitly related to the change in the index of refraction.
Conclusions In all, the results evidentially signify the interrelationship between the conformational changes and applied mechanical stress.

Keywords In-situ characterization · Dielectric elastic actuators · Terahertz spectroscopy · Polymer response

Introduction

Polymers continue to be an important class of materials for a plethora of load and non-load bearing applications, where polymers constitute a large portion of raw materials used in engineered products such as cellular phones, automobiles, and household goods, to name a few examples. The diversity of the sub-classification of polymers mirrors the variety of applications they are used in, including thermosets, thermoplastic, elastomers, biodegradable, and biopolymers. While this classification is not meant to be comprehensive nor exclusive, it is instead a shortlist to elude to the differences in the underlying molecular structure. Typical to any of these subclasses is the sensitivity to applied loads, regardless of the amplitude and directionality, which gives rise to molecular rearrangements that may be reversible or irreversible based on a balance between the strain energy imparted on the sample during loading and the activation energy required for irreversibility. The response of polymers is a scientific problem, extending over multiple time and length scales, that has gained attention from theoretical, experimental (in vitro experiments), and computational (in silico experiments) perspectives [1–6]. While the in silico experiments using Molecular Dynamics (or the like) approaches have proven to be essential tools in polymer science and engineering, continuum modeling remains essential not only to bridge the scale gap but also for practical applications. The reader is referred to the important contribution by Frenkel for a quick, yet insightful, review of the state of in silico research [6]. Here, the focus in on in vitro experimentation, but at the same time leveraging finite element analysis. The strain energy density is the result of the applied load and the deformed geometry, while the activation energy is an intrinsic property of the macromolecule that is fundamentally

---

✉ G. Youssef
gyoussef@sdsu.edu

[1] Experimental Mechanics Laboratory, Mechanical Engineering Department, San Diego State University, 5500 Campanile Drive, San Diego, CA 92182-1323, USA

connected to the bonds linking the backbone as well as the final arrangements of molecules after polymerization [7]. These quantities should be investigated simultaneously, given the relaxation behavior of polymers that negates the reversible contributions during the load history to reconcile the balance between strain and activation energies. The mechanical loading scenario and characterization methodology must be concurrently performed to capture the stress-induced macromolecule conformational arrangements.

It is well-known that the mechanical response of polymers exhibits a strong dependence on the molecular structure, the loading rate, and temperature such that thermosets, thermoplastics, and elastomers have unique stress-strain behavior that may span over a few hundred percentages of strains [7–9]. Elastomeric materials have a mechanical response with large stretch ratios, indicating a corresponding increase in the mechanical work done on the material. The mechanical work is captured by the strain energy calculated by taking the area under the stress-strain curve [10, 11]. There exist numerous ways of measuring strain where the selection of the method depends on (1) the strain percentage, e.g., large strain extensometer, (2) the scale with which optical methods are suitable for microscale measurements, and mechanical methods are feasible for meso and macro scale, and (3) the strain rate where the sampling rate is the deciding factor [12–14]. However, load application overwhelmingly relies on screw-driven or servo-hydraulic mechanisms in a load-frame type structure, but other experimental setups exist to investigate the mechanical response of materials under different strain rates [14]. Nonetheless, much of the strain and stress measurement/application methods are not conducive for integration in analytical chemistry instrumentation (discussed next) to elucidate the interrelationship between conformational changes and mechanical loading. Therefore, there is a need to develop a mechanism allowing the remote control of the state of stress without obscuring the observation site.

Dielectric elastomer actuators (DEAs) have been emerging as a viable actuation mechanism since their initial inception in the mid-1990s [15–18]. At its essence, DEAs leverage the compliant mechanical behavior of elastomers to achieve large deformation via the application of an electric field. When the latter is applied across the thickness of the actuator, it results in a localized compressive stress that affects the area surrounding the electrode region where the electric field was applied. The standard DEAs configuration can be round or diamond geometry such that the electrode area is either circular or rectangular, respectively. While the former is used to generate out-of-plane axial deformation, the latter is used to induce a sizable in-plane displacement. A common shortcoming of such actuator configuration for the purposes of in situ characterization of the polymer response is the electrode area, where the entire surface of the insulator is covered with a flexible conductive material. Therefore, the presence of the conductive material impedes the direct propagation of electromagnetic waves used for characterization. Here, an annulus electrode geometry is first investigated since it provides a generous unobstructed portion of the sample surface. It is worth noting that a biaxial state of stress can also be applied using an electric or mechanical camera shutter; however, the leaves of the mechanism may obstruct the propagating electromagnetic wave while posing a challenge in inducing precise, remote control of the deformation. Future research will focus on developing a new sample structure that uses an electrical shutter mechanism for in situ loading with spectroscopy.

To elucidate the molecular structure of polymers, scientists and engineers usually resort to ex-situ spectroscopy techniques such as microwave, Raman, and Fourier transform infrared spectroscopy (FTIR) operating between wavenumbers of 1 cm^{-1} and 10 cm^{-1} for the former, and 400 cm^{-1} and 14,000 cm^{-1} for the latter two [19–21]. The near and mid-infrared spectroscopy techniques are positioned for delineating the vibrational modes in the mid to high terahertz region, thus leaving the frequency vibrational modes associated with dynamic conformational changes in the low terahertz (THz) regime undetected. There is a well-known two-fold limitation of FTIR in the area of experimental and mechano-chemical characterization. First, FTIR is a surface spectroscopy technique with a penetration depth of 0.5 μm limiting the investigation to the first few layers of the material [22, 23]. Second, FTIR is unsuitable for integration of in situ dynamic mechanical characterizations since the sample must be stationary during the scan. On the other hand, terahertz based spectroscopy techniques are emerging as not only supplementary but also essential tools for probing the fingerprint region of materials with a higher resolution than the current state-of-the-art techniques [24–27]. Advantageous to the study of polymers (including biopolymers) is the safe level of electromagnetic radiation due to the low photon energy of the terahertz waves. That is to say, a propagating terahertz wave will be able to observe the intrinsic properties of matter without imparting any irreversible changes to the microstructure. Terahertz-based spectroscopy can be used to trace certain types of low-frequency vibrational characteristics, such as boson peaks [28, 29], and inter- and intramolecular vibrational modes including translational lattice vibrations of C-C bond in methylene groups at 2.2 THz, strong damping in the amorphous region at 1.5 THz, vibrations due to the intermolecular hydrogen bonding of polyhydroxy butyrate (PHB) at 2.49 THz, and vibrations due to the helical structure along fiber axis of PHB at 2.92 THz, to name a few [30–40]. Additionally, some mechanical properties have been investigated using terahertz, where the results are in excellent agreement with the current state-of-the-art (e.g., glass transition temperature using Differential Scanning Calorimetry) [41]. These hallmark characteristics of THz waves signify its suitability for integration in experimental mechanics studies, or in situ mechano-chemical experimentation.

The overarching objective of this research is to disseminate a new framework for the behavior of elastomeric polymers by leveraging the advantages of dielectric elastomer actuator structures and terahertz time-domain spectroscopy. The former was used as the sample structure that was subjected to remotely controlled varying levels of stresses, while the latter was concurrently used as a non-invasive, non-contact, non-destructive bulk spectroscopy technique. A novel analysis technique (not reported in the literature before for analysis of spectroscopic data) is presented and discussed.

Experimental Protocol

The DEA structure was used to apply a varying amplitude mechanical stress remotely by changing the applied voltage across two parallel electrodes, whereas the observation site was characterized using terahertz time-domain spectroscopy (THz-TDS) operating in the transmission mode. The following sections delineate the process used to prepare and characterize the sample using the non-invasive, non-contact, and non-destructive THz spectroscopy technique [42]. A finite element simulation was used to quantify the stress in the observation site by replicating the experimental conditions in the solver environment.

Test Sample Structure

The DEA sample consisted of an elastomeric dielectric insulator film with areas covered with a flexible conductive material to apply an electric field across the thickness selectively. A double-sided acrylic tape (3 M™ VHB™ Tape 4905) with an as-received thickness of 0.5 mm was manually stretched from an initial diameter of 25.4 mm to a final diameter of 76.2 mm (Fig. 1(a-b)), which resulted in a film thickness of 30 ± 6 μm (estimated from the time domain spectroscopy signals). Pre-straining the VHB has two advantages. First, by equi-biaxially stretching the film, the thickness consequently decreases; therefore, a lower applied voltage is required to obtain the same mechanical response. Second, pull-in instability can be avoided by pre-straining the film, which is kept in tension and effectively avoids buckling [43]. The pull-in failure mode occurs when the Maxwell pressure exceeds the third principal compressive stress of the elastomeric film. Plante and Dubowsky experimentally demonstrated that at a low pre-stretch ratio, the dominant failure mode for DEA is pull-in; however, at a high pre-stretch ratio, the dominant mode of failure is the dielectric breakdown [43]. While these two failure modes constitute the dominant mechanisms, material strength remains a concern based on the stretch rate and the pre-stretching percent [43].

After the elastomer film was stretched, it was then attached to a rigid plastic ring (Fig. 1(c)) with a 76 mm ID and 102 mm OD to avoid inducing unintended external strains during testing and data collection, while providing the necessary mechanical boundary conditions for proper operation of the actuator as discussed by Plante et al. [43]. Templates of the electrode configuration (Fig. 1(d)), including the lead locations, were prepared a priori by printing on a single-sided adhesive paper that was used as a mask during the application of the conductive graphene powder (AZ Laboratories, Ultra Conductive Graphene Powder) to both sides of the adhesive elastomer (Fig. 1(e-f)). Since the VHB film exhibits intrinsic tackiness, the conductive graphene powder stuck to the surface upon lightly tapping the powder using a foam applicator. Upon removal of the mask, the conductive electrodes were revealed (Fig. 1(g)), and two

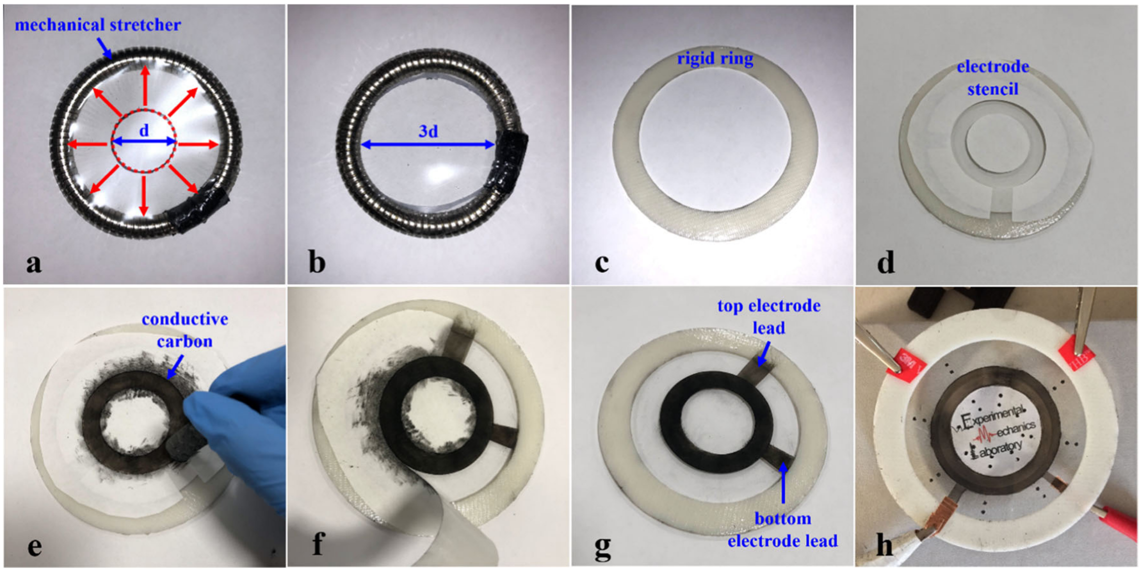

Fig. 1 Fabrication steps of the DEA samples showing the initial stretching, deposition of the electrode, and the application of the electric field during testing

copper tape strips, which were used as conductive leads to connect the applied field to the active electrode area, were then attached, (Fig. 1(h)). To actuate the DEA, a positive DC voltage was applied to one side of the VHB film while the other side was grounded using a DC power supply (Circuit Specialists, CSI3020X) and a high-voltage amplifier (Trek 609B-3). It is worth noting that the spot size of the THz wave is <<3 mm, which was focused at the middle of the sample (as discussed next). At 1 THz, the beam diameter of the terahertz propagating wave is ~300 µm. The remoteness of the THz characterization site with respect to the inner diameter of the electrode (38 mm) excludes the effect of the electric field on the spectroscopy THz wave. Furthermore, the self-boundedness of the electrode geometry indicates that the effect of the electric field is localized and limited to the active electrode area. Future research will focus on determining the bounds of applicability, relating the inner diameter of the electrode to the attributes of the THz wave. The applied voltage ranged from 0 V (used thereafter as the control) up to a voltage where the mechanical failure occurred (exhibited by the tearing of the VHB film due to localized wrinkling around the electrodes). On average, after performing the same testing protocol on seven different DEA samples, the mechanical failure corresponded to approximately 3250 V. Consistent with the previous investigation of Plante et al. and Wissler, this voltage and the pre-stretched ratio construed that the VHB was marginally stable to guard against pull-in failure [43, 44]. Moreover, the tearing of the film occurred due to the straightening and unfolding of the polymer chains [43]. It is worth noting that the applied voltage was increased at an increment of 250 V. In all, seven DEA samples were constructed and tested until mechanical failure, leading to the results summarized below.

Terahertz Time-Domain Spectroscopy (THz-TDS)

Terahertz time-domain spectroscopy (THz-TDS) was set up in transmission mode to facilitate the objective of in situ characterization of the stressed-area in the middle of the DEA sample, referred to as the observation site, where the VHB sample was situated at the focal point of the terahertz beam path with a spot size of 300 µm at 1 THz. It is important to note that the area of observation for the investigation using terahertz was not obstructed by the electrode materials or the leads (Fig. 1 shows a schematic of the DEA structure). A schematic of the transmission mode of the terahertz time-domain spectroscopy can also be seen in Fig. 2. Here, a pulsed femtosecond laser (Menlo Systems, ELMO 780 HP) with a pulse width of 100 fs was split into two different paths. The first path of the optical beam was focused on a photoconductive antenna transmitter (PCA Tx, TeTechS, T-Era-100A-800) to generate terahertz waves. The transmitter PCA was biased with a 45 Vpp square wave of 8000 Hz using a square wave generator (TeTechS Square Wave Generator). Using a series of off-axis parabolic (OAP) mirrors, the emitted terahertz beam was first focused onto the observation site of the sample. The refraction from the sample was then collimated and focused onto a photoconductive receiver antenna (PCA Rx, TeTechS, T-Era-20D40P-800) at the same instant the delayed second half of the optical beam activated the photoconductive receiver to convert the terahertz waves into a measurable electrical signal. The signal was measured using a low-noise amplifier (TeTechS, LNA) and was recorded using a built in-house data acquisition system. The collected data only underwent time-domain signal analysis given the limitation of frequency-domain based analysis [45], noting that the changes in the attributes of the terahertz pulse are implicitly associated with the complex index of refraction [45–58]. In here, the time-domain signals at each level of applied electric field were

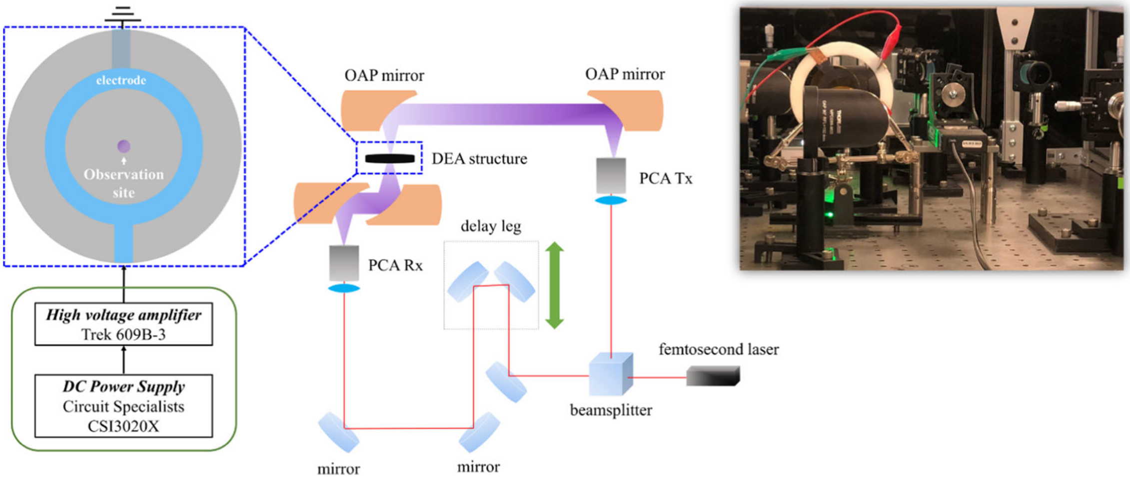

Fig. 2 Schematic of the non-contact, non-destructive, non-invasive THz-TDS setup operating in the transmission mode to provide evidence on the conformational changes due to the applied stress

analyzed to report the amplitude, full-width half maximum (FWHM), the 0–100% rise time, and the time-delay between the arrival of the reference time signal (referring to sample-free, baseline measurement) and the signal of the VHB at the observation site.

Stress Estimation Using Finite Element Simulation

The full-field state of stress at the observation site was estimated using a finite element simulation based on the Maxwell stresses developed under the surfaces of the electrode. That is to say, the application of an electric field across the thickness of the stretched VHB film resulted in the accumulation of opposite polarity charges at the electrode surfaces; hence, it attracted them closer to each other and induced localized compressive stresses that resulted in the reduction of the thickness under the electrode, which in turns causes an increase of the thickness of the middle area of the DEA. At the onset, a geometry analogous to that of the sample used in the physical testing (Fig. 3) was modeled in the finite element analysis (FEA) environment (Comsol Multi-Physics®) with a fixed constraint boundary condition applied to the most outer perimeter of the DEA sample resembling the rigid plastic ring used in the experiment to prevent rigid-body motion and external deformation. The boundary conditions are shown on Fig. 3. The VHB continuum was spatially discretized using a linear element with an average element size of 3 mm, whereas the thickness direction had at least two scaled elements. It is worth noting that the computational model can be simplified using axisymmetric assumptions, however, a full model was solved herein given the low required computational power. In addition, the computational framework may be used in future work for complex, nonsymmetrical electrode configurations.

Following the work of Pelrine [16], the electrostatic pressure (p_{es}) due to the applied electric field was converted a priori to an elastic compressive force (p_e) such that

$$p_e = -p_{es} = -\varepsilon_r \varepsilon_o \left({}^{U}/_{t}\right)^2 \tag{1}$$

where, ε_r is the relative dielectric constant of the VHB material (taken to be 3.2), ε_o is the free-space permittivity (8.85×10^{-12} F/m), U is the applied voltage ([0:250:3500] V) at the conductive electrodes across the thickness, and t is the thickness of the stretched film. The elastic compressive force (p_e) was then parametrically applied on the electrode area in lieu of the electric field. In short, Eq. 1 provides two alternative approaches to accomplish the same applied pressure via changing the electric field, namely, reducing the thickness or increasing the applied voltage. The latter approach was adopted herein.

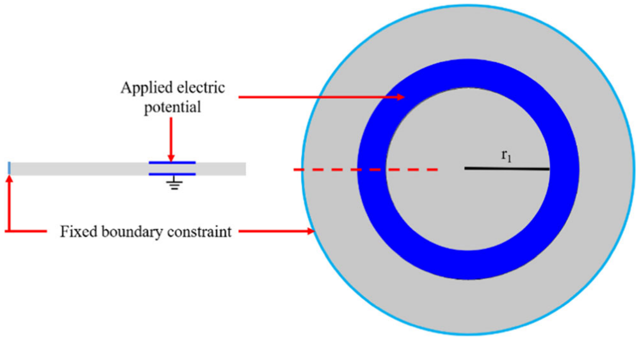

Fig. 3 Schematic representation of the FEA model showing the boundary conditions

Given the stretchability of the VHB materials, the above FEA model was then resolved by prescribing the material to obey hyperelasticity following the incompressible Yeoh model, whereas the strain energy density function (W) is given by

$$W = C_{10}(I_1-3) + C_{20}(I_1-3)^2 + C_{30}(I_1-3)^3 \tag{2}$$

where, I_1 is the first invariant of the left Cauchy-Green deformation tensor, and C_{10}, C_{20}, and C_{30} are material parameters determined by fitting the experimental data of the material to the stress expression derived from the energy potential, which were taken to be 80.3, −0.765, and 9.84×10^{-3} kPa, respectively [44, 59]. The third-order dependence on the first invariant is a characteristic advantage of the Yeoh model enabling higher accuracy while avoiding instabilities associated with other hyperelastic models, i.e., Yeoh model is Drucker stable since it has no dependence on the second invariant [7]. The latter is justified since the free energy of elastomers (as it is the case herein) is weakly dependent on the second invariant. In all, the FEA simulation is an uncoupled hyperelastic-electrostatic model, which was previously reported by Pelrine [16] to adequately represent the behavior of the DEA structure.

A final note is warranted about the time-dependent response of the VHB polymer undergoing constant stress over the scanning period. The strains of the VHB were shown experimentally by Wissler to reach a steady-state value of 120 s, which means the viscoelastic effect is negligible within the experimental time frame [44]. This supposition was further explained by Plante et al., explicating the inadequacy of DEAs for long-term actuation [43]. However, it is the objective of future research to systematically (experimentally and computationally) investigate the viscoelastic response of polymers (including VHB) using THz-TDS following the same framework established herein. The extraction of the dynamic mechanical properties of polymers will assist in the construction of a fully coupled, electrostatic, visco-hyperelastic simulation.

Results and Discussion

While it is well-known that the applied voltage on the electrode area in a DEA structure consequently results in mechanical stresses in both the active and passive areas, it was important to quantify the amplitude of the stresses, as well as its spatial distribution, corresponding to each operating condition based on the results from the FEA simulations. Figure 4 shows the results of the computational simulations elucidating the effective Von Mises stresses at two different applied electric fields. The Mises effective stress as a function of radial distance from the observation site towards the edge of the active electrode region at 2000 V and 3000 V are shown in Fig. 4(a) and (b), respectively. At the bottom panels of these figures, the Von Mises contour plots elucidate the full-field results of the stress. The effective stresses within the observation site as a function of the entire range of investigated electric field are also shown in Fig. 4(c). The full-field stress contour plots demonstrated nearly a uniform state of stress in the middle of the passive area, where the THz-TDS characterization took place. The Mises stress increased from 0.6 kPa at 1000 V to 2.5 kPa at 2000 V and finally reached a value of 7.3 kPa at 3000 V. However, it corresponded, not surprisingly, to approximately zero out-of-plane stresses regardless of the applied voltages which is due to the incompressibility of the VHB material and the resulting equi-biaxial stretching due to the symmetric geometry of the electrodes. Quantitatively, the plots in Fig. 4 shows the Mises stresses within the passive area varied between 7.3 kPa at the center to 7.2 kPa at 1.9 mm radially away from the center at 3000 V. This implies that the mechanical response was spatially uniform within the 3 mm maximum THz wave spot size used to interrogate the material. It is worth noting that the results shown in Fig. 4 omitted the effect of pre-stretching due to the sample fabrication process (Fig. 1) given the static nature of the simulation, where the time-dependent properties are suppressed. In other words, accounting for the pre-stretch stress would offset the result linearly.

The Maxwell stress under the active electrode region is directly proportional to the square of the applied electric field (Eq. 1), while the induced stresses at the observation site also exhibited nonlinear dependence on the stretch as described by the expression of the Yeoh Helmholtz free-energy potential in Eq. 2. Therefore, the reported Mises stresses showed a nonlinear dependence on the applied voltage. The results signify that the applied voltage can remotely control the amplitude of the stress (however, nonlinearly) in the passive area, as shown in Fig. 4(c). The stress contour plots also explicated the discontinuity behavior at the boundary between the active area where the electric field was applied and the surrounding passive areas, which were found to be in good agreement with the results in [43]. This can be leveraged in future research to concurrently explicate the dependence of the polymer response on the spatial variation of stress by developing novel electrode geometries. In all, as deduced from the contour plots shown in Fig. 4, the applied voltage in the active area resulted in uniform in-plane stresses that loaded the macromolecule chains in the vicinity of the observation site and effectively resulted in uncoiling and straightening of the chains, as discussed next.

Figure 5(a) shows the time-domain signals collected using the THz-TDS setup. The results include the signal without the DEA sample in the terahertz beam path (denoted as 'Reference'). It also encompasses the signals with the sample in the terahertz beam path while it was being subjected to an increasing voltage from 0 V (referred to as 'Control') to 3000 V. On the other hand, Fig. 5(b) plots the same time-domain signals but with a focus on the major terahertz peak arriving between 20 ps and 30 ps, clearly showing the drifting locations and changes in the amplitude of the peaks with varying applied voltage. As soon as the applied voltage increased beyond 3000 V, mechanical failure occurred, where the VHB sample was ripped into two pieces starting at the electrode area. That is, the localized induced mechanical stresses under the electrodes due to the applied electric field exceeded the intrinsic mechanical strength of the material, as discussed above. This indicates that mechanical stress is indeed developing and compressing at the observation site as demonstrated based on the FEA simulation results. Additional physical evidence of the generation of mechanical stress under the

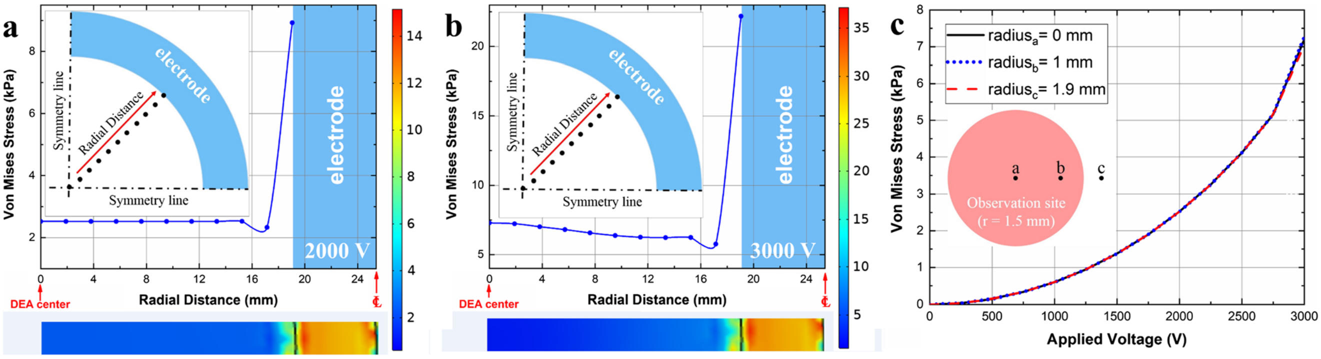

Fig. 4 Computational results from the DEA finite element simulation showing the (**a**) contour surface plots of the effective Von Mises stresses at different applied voltages, (**b**) Von Mises effective stress as function of the radial location from the center of the DEA to the edge of the electrode active area, and (**c**) Von Mises effective stress in the vicinity of the THz observation site as function of voltage

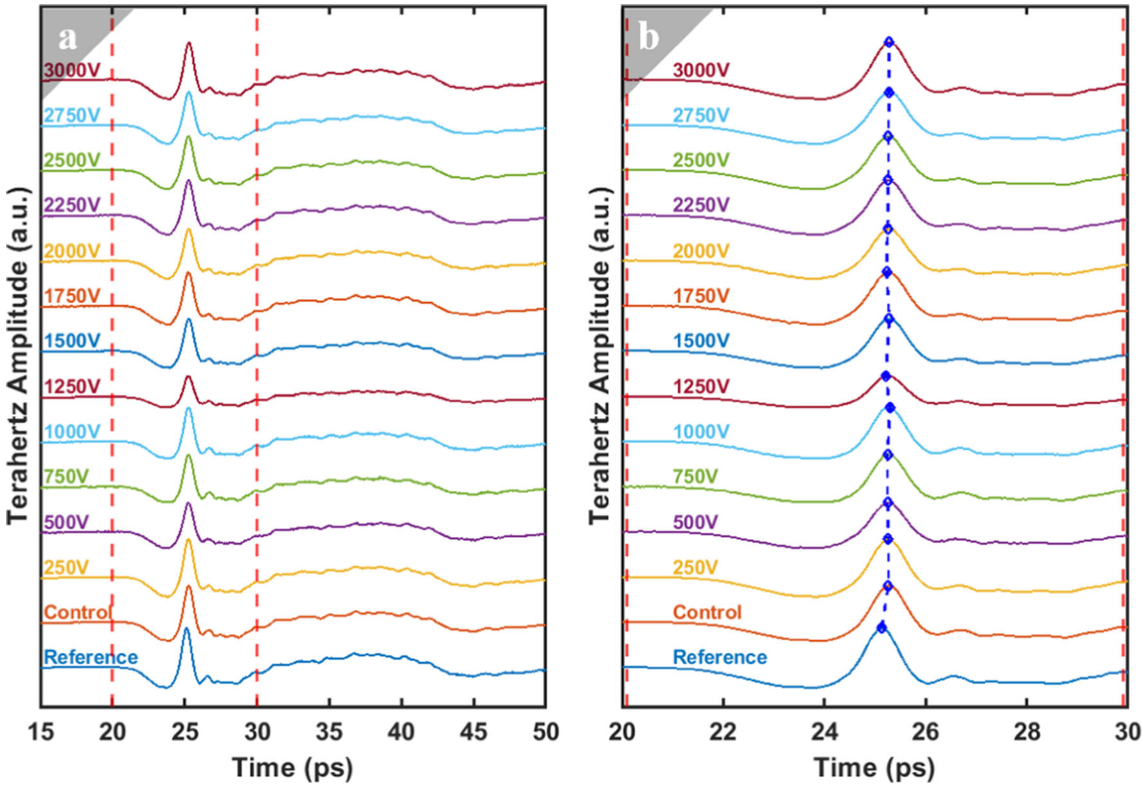

Fig. 5 Terahertz time-domain signals (**a**) of sample-free (reference), unbiased-sample (control), and at increasing applied voltage ranging from 250 V to 3000 V at an increment of 250 V with (**b**) truncated signals between 20 and 30 ps to show the shifting temporal locations of the peaks and changes in the signal characteristics

electrode was the dilation of the electrode surface, where the region between the inner and outer diameter of the electrode annulus widened (Fig. 6(b)) to 10.4 mm at 3000 V constituting a 30% increase from the 8.0 mm initial width when no electric potential was applied (Fig. 6(a)). The increase in the annulus width changed non-monotonically as a function of the voltage such that the width of the annulus increased to 8.35 mm, 8.48 mm, 8.86 mm, 9.79 mm, and 10.35 mm corresponding to 500 V, 1000 V, 1500 V, 2000 V, and 2500 V, respectively. The nonlinear widening of the electrode surface is consistent with the suppositions set forth by Eqs. 1 and 2. Notably, the distance between the markers (black dots on the surface of the DEA sample) located outside and inside the electrode area were also found to decrease, indicating that the external and internal areas were experiencing compressive stress. In all, the dilation of the electrode areas in response to the Maxwell stresses under the surface due to the oppositely poled electrodes coming closer together resulted in a uniform state of stress in the observation site. This points toward the validity of using the DEA framework as a method of applying mechanical stresses to elastomeric polymers without obscuring the observation site. Plante et al. analytically and experimentally demonstrated the development of stresses in the active area (i.e., under the electrode) as well as the passive area

Fig. 6. (**a**) starting DEA structure at 0 V showing the electrode configuration and (**b**) dilated electrode and stressed passive areas at 3000 V

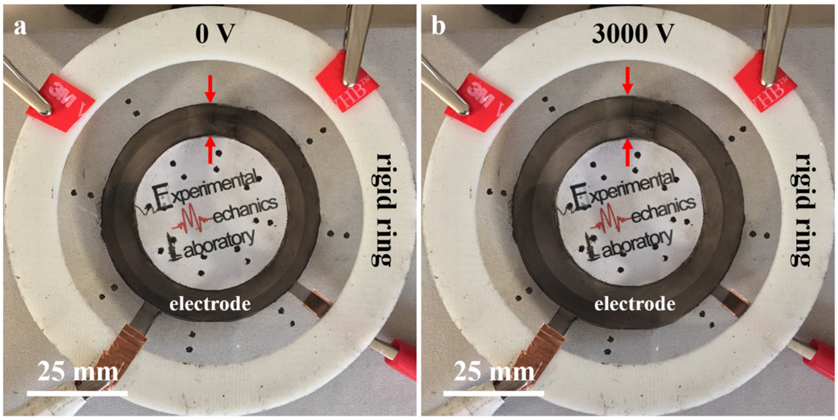

surrounding the electrode area [43]. Future research will focus on dynamically loading the sample using an AC electric field, which will result in cyclic mechanical stresses, i.e., giving rise to the viscoelastic response of the material. It is important to reiterate that the focus herein is not on the ability of the DEA to exert mechanical work, nor on investigating the failure, rather the objective is to demonstrate the effect of applied stress on the conformational entropy as discussed later.

The results, shown in Fig. 5, also point to changes in the signal characteristics based on the interactions between the propagating terahertz waves and the observation site of the DEA structure. Table 1 succinctly summarizes the extracted signal attributes as a function of the applied stresses in the electrode area (noting that stress is corresponding to the applied voltage across the thickness). Table 1 lists the estimated change in the thickness under the electrode and the estimated change in the thickness of the VHB film at the observation site as well as the amplitude, full-width at half-max (FWHM), rise time, and time delay of signal arrival between the corresponding applied voltage and the reference. First, the terahertz amplitude is found to change slightly (0.81 ± 0.03 a.u.) compared to the reference signal (0.88 a.u.), representing an 8% reduction in the amplitude. The initial reduction in the amplitude between the reference and control conditions is attributed to the change in the imaginary part of the index of refraction (i.e., absorption coefficient) due to the presence of the stretched VHB film. Regardless of the cellular microstructure of VHB, the resulting change in the signal characteristics are associated with the interaction of the propagating terahertz wave with the polymer solid occupying the observation site. As the voltage increases the compression of the thickness under the electrode will induce a stretching of the annular electrode width and consequently compress the area inside the inner diameter of the ring, thus, the thickness of the VHB at the observation site will increase. This can be confirmed by the FEA simulation results seen in Table 1. That is to say, the reported further change of the signal amplitude is due to the change in the sample complex index of refraction upon applying the mechanical stress. The compression of the VHB due to the radial stress at the observation site results in an increase in the refractive and the absorption coefficient. As discussed above, the self-boundedness of the annular electrode, the distance between the opposing electrodes, the insulation properties of the VHB polymer, and the remoteness of the observation site from the inner diameter of the electrode indicate the negligible effect of the applied electric field on the THz waves. The change in the amplitudes, whether from the reference sample-free to control (unbiased sample) or from the control to the biased conditions, are implicitly related to the change in the extinction coefficient since the reduction in the amplitude is a measure of damping.

In addition to the amplitude variations, the temporal characteristics of the waves are also dependent on the applied stresses, which can be connected to changes in the real part of the index of refraction. These temporal attributes include the FWHM, the rise time, and the delay time of arrival, shown graphically in Fig. 7(a), (b), and (c), respectively, based on the data from Table 1. A sudden change in the attributes of the time domain signals around 1250 V can be seen, where the FWHM and delay time were found to be 0.5104 ps and 0.08 ps, respectively. This change is thought to be associated with an initiated material instability resulting in a change in the mechanical deformation behavior under the electrode and at the observation site, after which, and once, the DEA structure re-equilibrated, the quasi-linear relationship between the applied voltages and induced stretches commenced. The peak width leading to the loading condition at 1250 V (14.1 kPa) continues to decrease due to an increase in the strains at the

Table 1 Summary of signal characteristics as a function of the applied voltage (mechanical stress) and estimated thickness (Δd_e is change in the thickness under the active electrode area and Δd_{os} change in the thickness at the observation site)

Applied potential (V)	% Δd_e	pressure (kPa)	% Δd_{os}	Terahertz Amplitude (a.u.)	FWHM (ps)	Peak Rise Time (ps)	Delay (ps)
0	0.00	0.00	0.00	0.8060	0.5113	0.3491	0.0700
250	0.04	−0.56	0.00	0.8039	0.5087	0.3460	0.0633
500	0.13	−2.25	0.04	0.8205	0.5071	0.3434	0.0667
750	0.29	−5.07	0.07	0.8249	0.5069	0.3441	0.0750
1000	0.50	−9.01	0.13	0.8279	0.5077	0.3441	0.0875
1250	0.80	−14.07	0.20	0.8272	0.5104	0.3451	0.0833
1500	1.16	−20.26	0.29	0.8310	0.5085	0.3459	0.0667
1750	1.61	−27.58	0.39	0.8331	0.5088	0.3464	0.0767
2000	2.14	−36.02	0.52	0.8325	0.5090	0.3457	0.0733
2250	2.75	−45.59	0.68	0.8361	0.5104	0.3452	0.0800
2500	3.48	−56.28	0.86	0.8365	0.5097	0.3453	0.0867
2750	4.32	−68.10	1.07	0.8380	0.5055	0.3439	0.0750
3000	5.30	−81.05	1.55	0.8511	0.5060	0.3492	0.0667

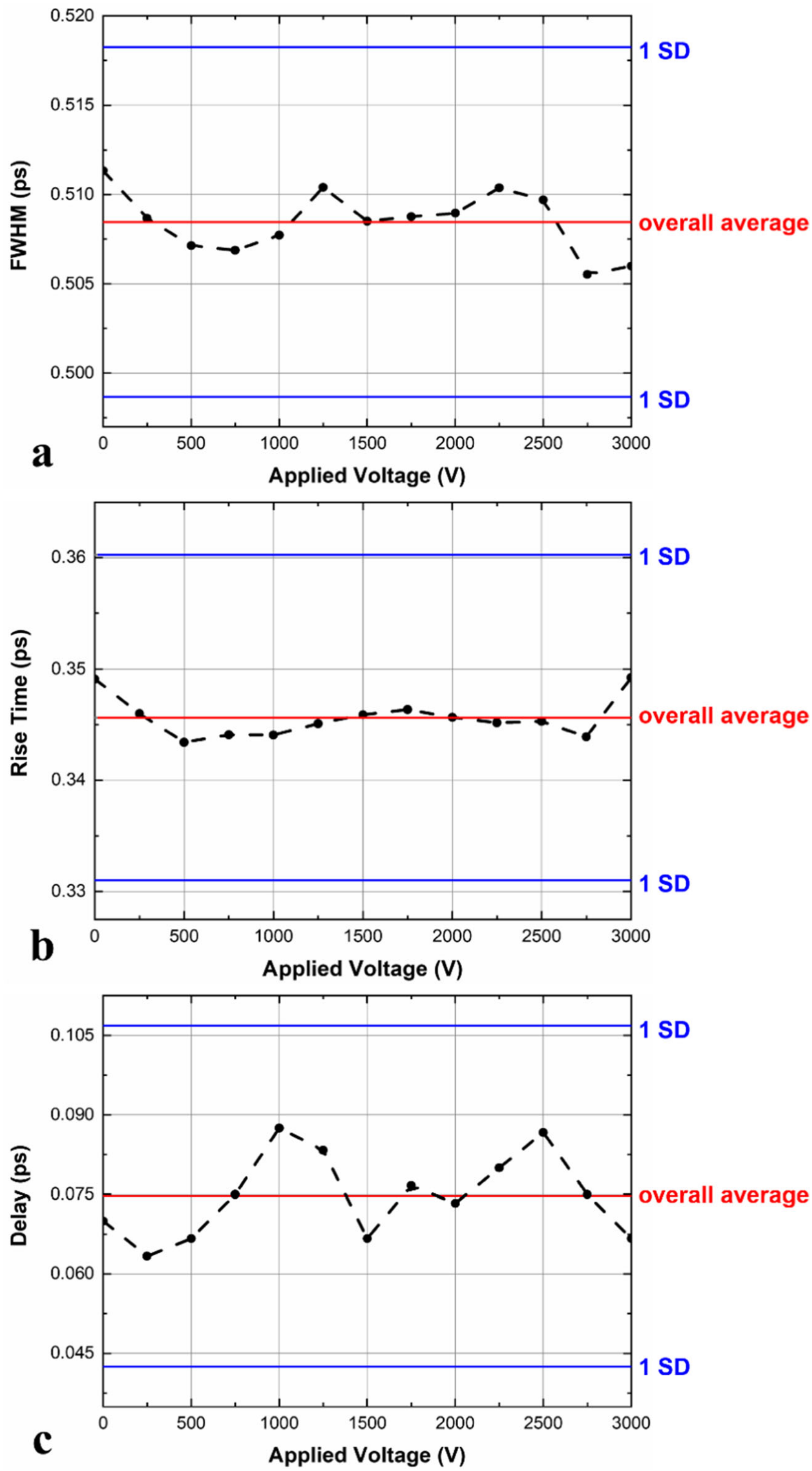

Fig. 7 The temporal characteristics of the terahertz time-domain signals including (**a**) full-width at half-max (FWHM), (**b**) time rise, and (**c**) delay time of arrival based on data from Table 1

observation site, which, in turn, affects the local values of the strain energy. To better elucidate the underlying molecular changes, the FEA analysis should be coupled with molecular modeling and simulation to discern associated entropic evolution from conformational changes. This will be the focus of future in silico studies. The broadening in the peak width at 14.1 kPa also corresponds to inflection of the delay time, where the difference between the arrival of the reference (sample-free) wave and the arrival of the terahertz wave after passing through the stressed-sample is found to be 0.0833 ps. This suggests a drop in the index of refraction (i.e., getting closer to the index of air). The real part of the index of refraction can be calculated from the delay time (Δt) between the initial arrival of the reference wave and the sample signal such that $n = 1 + (c\Delta t/\delta)$, where c is the speed of light in vacuum and δ is the thickness of the VHB film. Therefore, any changes in the delay time signify a variation in the index of refraction (n). Using the data in Table 1, the index of refraction is estimated to be 1.71, which is in good agreement with the published index by the manufacturer by considering the stretching effects on the optical properties of the material.

Due to the limitation of the existing state-of-the-art analysis techniques, terahertz time-domain signals of ultrathin samples, as it is the case herein, are not suitable for transformation to the frequency domain based on the limits set by Scheller et al. as a function of frequency resolution, and bandwidth of the signal [45]. In Fourier Transform based analysis technique, Scheller et al. discussed that the prerequisite for the lower bound of the sample thickness using terahertz spectroscopy is defined based on, $\delta_{min} = c/2n\Delta f$, where, the refractive index is taken here to be 1.79 [60] and Δf is the bandwidth (estimated to be 1.5 THz for our setup). That is, the time-domain signal from a sample with a thickness below 56 μm cannot be effectively analyzed in the frequency domain. This is a shortcoming of the post-processing step rather than the spectroscopy technique itself. Therefore, in an attempt to further elucidate the underlying changes in the microstructure, we abandon the Fourier Transform approach and adopt (for the first time in the analysis of spectroscopic data) the Hilbert-Huang transform (HHT) through a sifting process, also known as Empirical Mode Decomposition (EMD) [61, 62]. EMD deconvolves the signal into its Intrinsic Mode Functions (IMF), whereas each IMF is monotonic, including the signal information at a single frequency component but still represented in terms of time. The first three IMFs of each investigated condition are represented in Fig. 8, where it is essential to note that IMFs pertaining to high-frequency noise were omitted and replaced by the next mode.

The resulting intrinsic mode functions shown in Fig. 8 are the first three oscillation modes embedded in the signals. Generally, the first and second intrinsic mode functions of the THz-TDS signals exhibit distinct behaviors expressed by an individual wave packet centered approximately at 25 ps with notable changes in the attributes of each wave packet. The apparent increase in the amplitude of the wave in the first modes compared to the amplitude of the reference signal is attributed to the change in the index of refraction due to the presence of the VHB samples in the terahertz wave path. The shape and characteristics of the wave packet at 1250 V continue to support the previous observations of an inflection point in the response, where the wave packets at higher levels of stresses (i.e., voltage) are distinctively different from their low stresses counterparts. Finally, the third intrinsic mode function for the reference signal contains higher energy, whereas the 3rd IMFs of the VHB sample appear to represent the trend of the data rather than an oscillation mode. Indeed,

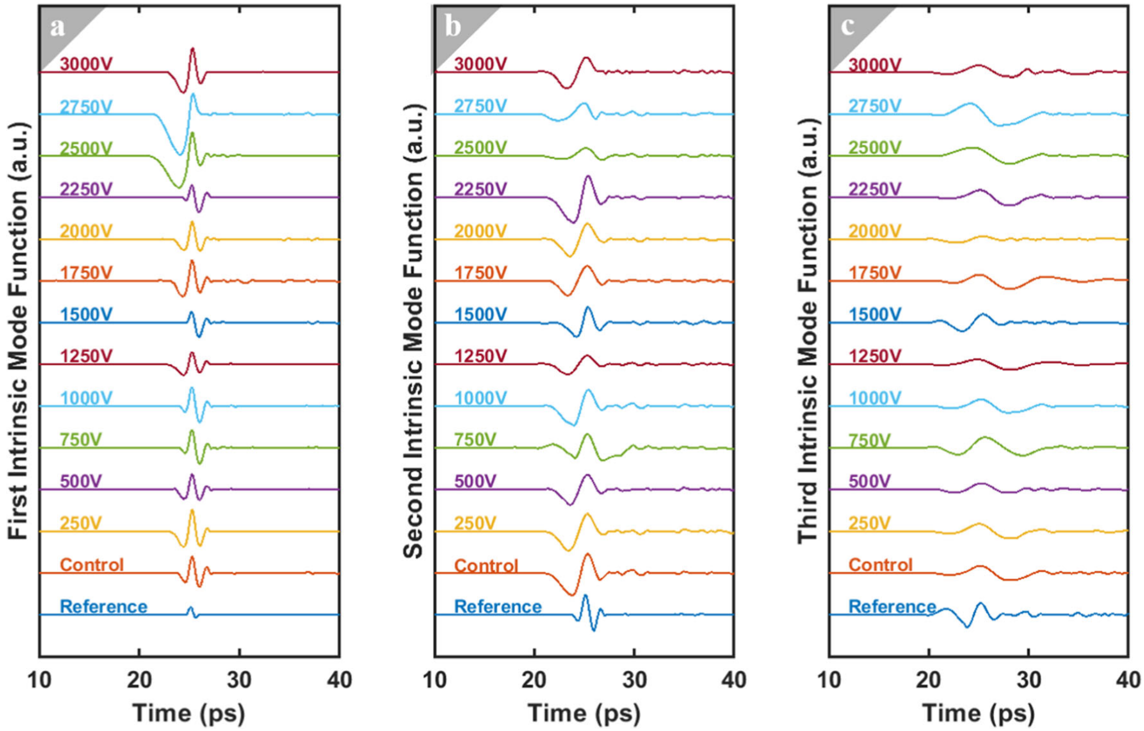

Fig. 8 First (**a**), Second (**b**), and Third (**c**) intrinsic mode functions (high-frequency noise modes were omitted) of the THz time-domain signal elucidating the difference in the fundamental characteristics of the samples' waveforms as a function of applied voltage in comparison to the sample-free reference and zero-voltage conditions

the concentration of the energy in the first and second mode functions is in excellent agreement with the association of the conformational orders, as discussed above, given that higher frequencies (higher energy) are linked to lower-order modes. Future research will focus on establishing a strong correlation between the results of the IMFs and the optical and electrical properties of polymers. The correlation between conformational changes in conjunction with loading-based variation in the time-domain signals, or IMFs, stems from the essence of the spectroscopic data and its association with molecular vibrational modes. The latter is detected within a frequency range based on the interaction of the propagating electromagnetic wave with the test structure, resulting, for example, in oscillations due to bond stretching or bending. The vibrations are usually elucidated using spectral analysis, which was not possible herein due to the current bandwidth limitations, as discussed before.

At the outset, using the DEA structure was found to be a reliable way to remotely apply a uniform state of stress without obscuring the observation site, hence, providing a pathway to non-invasively and non-destructively interrogate the polymer using non-contact terahertz time-domain spectroscopy technique. All reported loadings thus far were normal stresses due to the configuration of the active electrode area; however, the mechanical response of polymers has been shown to exhibit sensitivity to shear deformation due to the sliding and rearrangement of chains in response to mechanical work. To remedy this shortcoming of our approach, we propose a novel electrode area configuration that selectively gives rise to shear and normal stresses on the same or different locations within the same DEA structure. As discussed before, the actuation performance of the DEA is not the objective here but rather to use the coupling between electrostatic and mechanics to remotely and systemically apply mechanical stresses.

Conclusion

The eminence of polymers in a plethora of load-bearing engineering applications necessitates the fundamental understanding of the concurrent effect of stress on the conformational changes in the macromolecule. A new experimental mechanics framework was introduced to investigate the mechanical response of polymers using THz-TDS while the sample was under varying levels of stresses that were remotely controlled using an input voltage. A localized Maxwell stress due to the attraction of opposing polarity electrodes resulted in the expansion of the thickness of the unobscured remote observation area that was interrogated by terahertz waves. The results provide physical evidence on the effect of conformational changes of polymers through analyses of time-domain signals that signified changes in the optical properties of the sample (index of refraction). HHT was introduced to decompose the time-domain signals into its fundamental modes, hence, decoying the shortcomings of the current state-of-the-art analysis technique in the frequency domain. Future research will focus on the dynamic response of polymers by subjecting the samples to alternating mechanical stress as well as on establishing the predictive and correlative relationship between the output of the Hilbert-Huang transform and the optical properties of the material.

Acknowledgements The research leading to these results was supported in part by the United States Department of Defense under Grant Agreement No. W911NF1410039 and W911NF1810477. The authors are grateful to the guidance of Dr. Roshdy Barsoum of the Office of Naval Research. The research was also supported by the National Science Foundation under Award No. 1925539.

Compliance with Ethical Standards

Ethical Statement/Conflict of Interest The authors confirm that the manuscript has only been submitted to the Journal of Experimental Mechanics for consideration. The authors contributed equally to the research leading to the publication as well as to the composition of the manuscript. The authors further report no conflict of interest.

References

1. Kremer K, Müller-Plathe F (2002) Multiscale simulation in polymer science. Mol Simul 28:729–750. https://doi.org/10.1080/08927020211000002458
2. Gartner TE, Jayaraman A (2019) Modeling and simulations of polymers: a roadmap. Macromolecules 52:755–786. https://doi.org/10.1021/acs.macromol.8b01836
3. Ngai KL, Plazek DJ (1995) Identification of different modes of molecular motion in polymers that cause thermorheological complexity. Rubber Chem Technol 68:376–434
4. Shenogina NB, Tsige M, Patnaik SS, Mukhopadhyay SM (2012) Molecular modeling approach to prediction of thermo-mechanical behavior of thermoset polymer networks. Macromolecules 45:5307–5315. https://doi.org/10.1021/ma3007587
5. Glotzer SC, Paul W (2002) Molecular and mesoscale simulation methods for polymer materials. Annu Rev Mater Sci 32:401–436. https://doi.org/10.1146/annurev.matsci.32.010802.112213
6. Frenkel D (2013) Simulations: the dark side. Eur Phys J Plus 128: https://doi.org/10.1140/epjp/i2013-13010-8
7. Bergstrom J (2015) Mechanics of solid polymers theory and computational modeling. Matthew Deans
8. Arruda EM, Boyce MC (1993) A three-dimensional constitutive model for the large stretch behavior of rubber elastic materials. J Mech Phys Solids 41:389–412. https://doi.org/10.1016/0022-5096(93)90013-6
9. Flory PJ (1953) Principles of polymer chemistry. Cornell Unversity Press
10. Bower AF (2010) Applied mechanics of solids. CRC Press
11. Timoshenko S, Goodier JN (1951) Theory of elasticity. McGraw-Hill book Company
12. Youssef G, Gupta V (2012) Dynamic response of polyurea subjected to nanosecond rise-time stress waves. Mech Time-Depend Mat 16(3):317–328
13. Youssef G, Gupta V (2012) Dynamic tensile strength of polyurea. J Mater Res 27:494–499. https://doi.org/10.1557/jmr.2011.405

14. Sharpe W (2008) Springer handbook of experimental solid mechanics. Springer Science+Business Media, Baltimore
15. Kornbluh RD, Pelrine RE, Joseph J (1995) Elastomeric dielectric artificial muscle actuators for small robots. Proc Mater Res Soc Symp 600:119–130
16. Pelrine RE, Kornbluh RD, Joseph JP (1998) Electrostriction of polymer dielectrics with compliant electrodes as a means of actuation. Sensors Actuators A Phys 64:77–85. https://doi.org/10.1016/S0924-4247(97)01657-9
17. Kornbluh R, Pelrine R, Joseph J, Pei Q, Chiba S (2000) Ultra-high strain response of elastomeric polymer dielectrics. Mater Res Soc Symp - Proc 600:119–130. https://doi.org/10.1557/proc-600-119
18. Full J, Meijer K (2000) Artificial muscles versus natural actuators from frogs to flies 3987:2–9
19. Harris D, Bertolucci M (1978) Symmetry and spectroscopy. Oxford University Press, Inc.
20. Siesler HW, Holland-Moritz K (1980) Infrared and Raman spectroscopy of polymers. Marcel Dekker, Inc.
21. Koenig JL (1999) Spectroscopy of polymers. Elsevier
22. Götz A, Nikzad-Langerodi R, Staedler Y, Bellaire A, Saukel J (2020) Apparent penetration depth in attenuated total reflection Fourier-transform infrared (ATR-FTIR) spectroscopy of Allium cepa L. epidermis and cuticle. Spectrochim Acta - Part A Mol Biomol Spectrosc 224:1–6. https://doi.org/10.1016/j.saa.2019.117460
23. Gaigneaux A, Goormaghtigh E (2013) A new dimension for cell identification by FTIR spectroscopy: depth profiling in attenuated total reflection. Analyst 138:4070–4075. https://doi.org/10.1039/c3an00193h
24. Lee YS (2009) Principles of terahertz science and technology
25. Coutaz J-L, Garet F, Wallace VP (2018) Principles of Terahertz time-domain spectroscopy: an introductory textbook. CRC Press
26. Saeedkia D (ed) (2013) Handbook of terahertz technology for imaging, sensing, and communications. Elsevier
27. Dexheimer SL (2008) Terahertz spectroscopy: principles and applications. Taylor & Francis, Boca Raton
28. Terao W, Mori T, Fujii Y, Koreeda A, Kabeya M, Kojima S (2018) Boson peak dynamics of natural polymer starch investigated by terahertz time-domain spectroscopy and low-frequency Raman scattering. Spectrochim Acta - Part A Mol Biomol Spectrosc 192:446–450. https://doi.org/10.1016/j.saa.2017.11.051
29. Iijima Y, Mori T, Kojima S, et al (2018) Terahertz Time-Domain Spectroscopy and Low-Frequency Raman Scattering of Boson Peak Dynamics of Lithium Borate Glasses. Int Conf Infrared, Millimeter, Terahertz Waves, IRMMW-THz 2018-Septe:4–5. https://doi.org/10.1109/IRMMW-THz.2018.8510433
30. Bank MI, Krimm S (1968) Lattice studies of cristalline strucure of polyethylene. J Appl Phys 39:4951–4958
31. Fuse N, Sato R, Mizuno M, Fukunaga K, Itoh K, Ohki Y (2010) Observation and analysis of molecular vibration modes in polylactide at terahertz frequencies. Jpn J Appl Phys 49:1024021–1024028. https://doi.org/10.1143/JJAP.49.102402
32. Hoshina H, Morisawa Y, Sato H, Kamiya A, Noda I, Ozaki Y, Otani C (2010) Higher order conformation of poly(3-hydroxyalkanoates) studied by terahertz time-domain spectroscopy. Appl Phys Lett 96:3–6. https://doi.org/10.1063/1.3358146
33. Hoshina H, Morisawa Y, Sato H, Minamide H, Noda I, Ozaki Y, Otani C (2011) Polarization and temperature dependent spectra of poly(3-hydroxyalkanoate)s measured at terahertz frequencies. Phys Chem Chem Phys 13:9173–9179. https://doi.org/10.1039/c0cp02435j
34. Neu J, Nikonow H, Schmuttenmaer CA (2018) Terahertz spectroscopy and density functional theory calculations of dl -Norleucine and dl -methionine. J Phys Chem A 122:5978–5982. https://doi.org/10.1021/acs.jpca.8b04978
35. Neu J, Stone EA, Spies JA, Storch G, Hatano AS, Mercado BQ, Miller SJ, Schmuttenmaer CA (2019) Terahertz spectroscopy of Tetrameric peptides. J Phys Chem Lett 10:2624–2628. https://doi.org/10.1021/acs.jpclett.9b01091
36. Neu J, Schmuttenmaer CA (2020) Terahertz spectroscopy and density functional theory investigation of the dipeptide L-Carnosine. J Infrared, Millimeter, Terahertz Waves 41:1366–1377. https://doi.org/10.1007/s10762-019-00636-7
37. Kister G, Cassanas G, Vert M (1998) Effects of morphology, conformation and configuration on the IR and Raman spectra of various poly(lactic acid)s. Polymer (Guildf) 39:267–273. https://doi.org/10.1016/S0032-3861(97)00229-2
38. Cunningham PD, Valdes NN, Vallejo FA, Hayden LM, Polishak B, Zhou XH, Luo J, Jen AKY, Williams JC, Twieg RJ (2011) Broadband terahertz characterization of the refractive index and absorption of some important polymeric and organic electro-optic materials. J Appl Phys 109:0–5. https://doi.org/10.1063/1.3549120
39. Zhao Y, Li Z, Liu J, Hu C, Zhang H, Qin B, Wu Y (2018) Intermolecular vibrational modes and H-bond interactions in crystalline urea investigated by terahertz spectroscopy and theoretical calculation. Spectrochim Acta - Part A Mol Biomol Spectrosc 189:528–534. https://doi.org/10.1016/j.saa.2017.08.041
40. Podzorov A, Gallot G (2010) Density of states and vibrational modes of PDMS studied by terahertz time-domain spectroscopy. Chem Phys Lett 495:46–49. https://doi.org/10.1016/j.cplett.2010.06.050
41. Wietzke S, Jansen C, Jung T et al (2009) Terahertz time-domain spectroscopy as a tool to monitor the glass transition in polymers. Optics Express 17:19006–19014
42. Youssef G, Huynh NU Integrated temperature-controlled, ultrahigh strain rate loading, and spectroscopy apparatus for dynamic characterization of materials. U.S Patent Application No. 62/929,586
43. Plante JS, Dubowsky S (2006) Large-scale failure modes of dielectric elastomer actuators. Int J Solids Struct 43:7727–7751. https://doi.org/10.1016/j.ijsolstr.2006.03.026
44. Wissler M (2007) Modeling dielectric elastomer actuators (Doctoral dissertation, ETH Zurich)
45. Scheller M (2014) Data extraction from terahertz time domain spectroscopy measurements. J Infrared Millimeter Terahertz Waves 35:638–648. https://doi.org/10.1007/s10762-014-0053-4
46. Dhillon SS, Vitiello MS, Linfield EH, Davies AG, Hoffmann MC, Booske J, Paoloni C, Gensch M, Weightman P, Williams GP, Castro-Camus E, Cumming DRS, Simoens F, Escorcia-Carranza I, Grant J, Lucyszyn S, Kuwata-Gonokami M, Konishi K, Koch M, Schmuttenmaer CA, Cocker TL, Huber R, Markelz AG, Taylor ZD, Wallace VP, Axel Zeitler J, Sibik J, Korter TM, Ellison B, Rea S, Goldsmith P, Cooper KB, Appleby R, Pardo D, Huggard PG, Krozer V, Shams H, Fice M, Renaud C, Seeds A, Stöhr A, Naftaly M, Ridler N, Clarke R, Cunningham JE, Johnston MB (2017) The 2017 terahertz science and technology roadmap. J Phys D Appl Phys 50:043001. https://doi.org/10.1088/1361-6463/50/4/043001
47. Naito K, Kagawa Y, Utsuno S, Naganuma T, Kurihara K (2009) Dielectric properties of woven fabric glass fiber reinforced polymer-matrix composites in the THz frequency range. Compos Sci Technol 69:2027–2029. https://doi.org/10.1016/j.compscitech.2009.04.001
48. Fischer BM, Wietzke S, Reuter M, Peters O, Gente R, Jansen C, Vieweg N, Koch M (2013) Investigating material characteristics and morphology of polymers using terahertz technologies. IEEE Trans Terahertz Sci Technol 3:259–268. https://doi.org/10.1109/TTHZ.2013.2255916
49. Fedulova EV, Nazarov MM, Angeluts AA et al (2012) Studying of dielectric properties of polymers in the terahertz frequency range. Saratov Fall Meet 2011 Opt Technol Biophys Med XIII 8337:83370I. https://doi.org/10.1117/12.923855

50. Wietzke S, Jansen C, Reuter M, Jung T, Kraft D, Chatterjee S, Fischer BM, Koch M (2011) Terahertz spectroscopy on polymers : a review of morphological studies. J Mol Struct 1006:41–51. https://doi.org/10.1016/j.molstruc.2011.07.036
51. Jepsen PU, Fischer BM (2005) Dynamic range in terahertz time-domain transmission and reflection spectroscopy. Opt Lett 30:29–31. https://doi.org/10.1364/ol.30.000029
52. Withayachumnankul W, Fischer BM, Abbott D (2008) Material thickness optimization for terahertz time-domain spectroscopy. Opt Soc Am 16:7382–7396
53. Withayachumnankul W, Fischer BM, Lin H, Abbott D (2008) Uncertainty in terahertz time-domain spectroscopy measurement. J Opt Soc Am B 25:229–247. https://doi.org/10.1007/s10762-016-0318-1
54. Pupeza I, Wilk R, Koch M (2007) Highly accurate optical material parameter determination with THz time-domain spectroscopy 15: 1598–1609
55. Li X, Hong Z, He J, Chen Y (2010) Precisely optical material parameter determination by time domain waveform rebuilding with THz time-domain spectroscopy. Opt Commun 283:4701–4706. https://doi.org/10.1016/j.optcom.2010.06.088
56. Scheller M (2011) Real-time terahertz material characterization by numerical three-dimensional optimization. Opt Express 19:10647–10655. https://doi.org/10.1364/oe.19.010647
57. Bernier M, Garet F, Coutaz JL (2013) Precise determination of the refractive index of samples showing low transmission bands by THz time-domain spectroscopy. IEEE Trans Terahertz Sci Technol 3:295–301. https://doi.org/10.1109/TTHZ.2013.2247793
58. Duvillaret L, Garet F, Coutaz J-L (1999) Highly precise determination of optical constants and sample thickness in terahertz time-domain spectroscopy. Appl Opt 38:409–415. https://doi.org/10.1364/ao.38.000409
59. Yeoh OH (1993) Some forms of the strain energy function for rubber. Rubber Chem Technol 66:754–771
60. Data T (2011) VHB ™ Tapes product description :
61. Huang NE, Wu Z, Long SR, Arnold KC, Chen X, Blank K (2009) On instantaneous frequency. Advances in adaptive data analysis. 2009 Apr;1(02):177–229. https://doi.org/10.1142/S1793536909000096
62. Huang NE, Shen S (2014) Hilbert-Huang transform and its applications, vol 16. World Scientific